

Permeability anisotropy induced by the shear displacement of rough fracture walls.

H. Auradou,¹ G. Drazer,² J.P. Hulin,¹ and J. Koplik²

H. Auradou, Laboratoire Fluide, Automatique et Systèmes Thermiques, UMR No. 7608, CNRS, Université Paris 6 and 11, Bâtiment 502, Université Paris Sud, 91405 Orsay Cedex, France.
(auradou@fast.u-psud.fr)

¹Laboratoire Fluide, Automatique et Systèmes Thermiques, UMR No. 7608, CNRS, Université Paris 6 and 11, Bâtiment 502, Université Paris Sud, 91405 Orsay Cedex, France.

²Benjamin Levich Institute and Department of Physics, City College of the City University of New York, New York, NY 10031.

Abstract. The permeability anisotropy that results from a shear displacement \vec{u} between the complementary self-affine walls of a rough fracture is investigated. Experiments in which a dyed fluid displaces a transparent one as it is radially injected into a transparent fracture exhibit a clear anisotropy in the presence of shear displacements, and allow us to estimate the ratio of the permeabilities for flows parallel and perpendicular to \vec{u} . A simple model which accounts for the development of channels perpendicular to \vec{u} qualitatively explains these results, and predicts a permeability decreasing (increasing) linearly with the variance of the aperture field for flow parallel (perpendicular) to the shear displacement. These predictions are then compared to the results of numerical simulations performed using a lattice-Boltzmann technique and to the anisotropies measured in displacement experiments.

1. Introduction

Subsurface fluid flow in low-permeability geological formations occurs primarily through networks of fractures [NAS, 1996; Adler and Thovert, 1999; Sahimi, 1995]. In order to model such systems, one needs to understand flow in single fractures which are the building blocks of the network. Among the many parameters which influence fluid motion at this scale, we focus here on the geometry of the fractures, specifically on the correlations between the roughness of the surfaces of the two opposite walls. A shear displacement of the latter alters these correlations and previous laboratory measurements demonstrated that it also affects the permeability, through variations of the local aperture of the fracture due to the wall roughness [Plouraboué *et al.*, 2000; Olsson and Brown, 1993].

In related experiments, a higher permeability was measured for flow perpendicular to the shear displacement than parallel to it [Gentier *et al.*, 1997; Yeo *et al.*, 1998]. Numerical studies found a similar behavior on explicitly anisotropic rough surfaces generated numerically [Thompson and Brown, 1991]; an indication of such anisotropic permeability was also observed in a previous work on self-affine fracture [Drazer and Koplik, 2002]. The purpose of the present paper is to combine experiments, systematic numerical simulations, and analytic arguments to understand the permeability anisotropies that are induced by shear displacements of rough fracture walls.

A key geometrical feature of the fracture surfaces studied in this work is their statistical scale invariance known as *self-affinity* [Mandelbrot, 1983; Feder, 1988]. The analysis of the surfaces of both fault and fresh fractures has established that their roughness cannot be described by a finite set of typical wavelength values, but instead is self-affine. A self-

affine surface is one that is *statistically* unchanged under the scaling relation: $x \rightarrow \lambda x$, $y \rightarrow \lambda y$ and $h(x, y) \rightarrow \lambda^\zeta h(x, y)$. ((x, y) are coordinates in the mean surface plane, $h(x, y)$ is the local height of the surface, and ζ is known as the Hurst exponent.) The self-affine character of the fracture surfaces has been observed, over a significant range of length scales, in a broad variety of materials and for both natural and man-made fractures [Bouchaud, 2003]. In the case of fractured rocks, such as granite or basalt rocks, the Hurst exponent is found to be $\zeta \approx 0.8 \pm 0.05$ over a broad range of length scales [Bouchaud, 2003], although values near 0.5 are found in other rocks [Boffa, 1998].

The key consequence of self-affinity in our context is the following scaling law for the variance of the surface heights:

$$\langle [h(\vec{x} + \vec{\lambda}) - h(\vec{x})]^2 \rangle \sim |\vec{\lambda}|^{2\zeta}, \quad (1)$$

which implies long-range correlations in the height-to-height fluctuations, and should be contrasted with the fluctuations in surface height that would arise from a random field with a characteristic correlation length, which ultimately leads to a linear growth of the variance ¹. It will be seen that these correlations strongly affect the spatial aperture distribution of the rough fractures studied in the present work, and therefore, the flow inside them.

In both experiments and numerical studies, we shall consider model fractures, made of two complementary rough self-affine surfaces: two perfectly matching surfaces separated by a distance a_0 in the direction normal to their common mean plane and, in general, subject to a shear displacement \vec{u} parallel to this mean plane. In all cases, the gap between surfaces is large enough so that the two walls do not touch, thereby avoiding the effects of shear-induced dilation of the fracture gap on its permeability.

The experiments were performed using transparent models fabricated with moldings of actual rocks. In the experiments, a dye is injected radially from a point of the fracture and the anisotropy in the permeability is computed from that of the injection patterns. Only the ratio of the highest and lowest permeabilities can be determined in this way, but not their absolute values. These experiments are therefore appropriately complemented by numerical simulations which, in addition to the permeability, provide the complete flow field. The lattice Boltzmann technique has been used since it is convenient for determining the velocity field in these complex geometries [Drazer and Koplik, 2002; Kim *et al.*, 2003].

The paper is organized as follows: in Sec. 2.1, the laboratory procedure used to obtain the transparent cast of the fractured rock is described as well as the characterization of the surface roughness. The experimental set-up and the image analysis methods are described in Sec. 2.2. In order to explain the experimental results described in Sec. 3, a theoretical analysis of the relation between the aperture field and the observed anisotropy in the permeability is developed in Sec. 4. The scaling laws obtained in this way are then compared to numerical simulations in Secs. 5 and 6. The same approach is finally applied to the experimental data in Sec. 7.

2. Experimental set-up and procedure

2.1. Model fracture and flow set-up

The experiments were performed on transparent moldings of fractured granite blocks extracted from a quarry in Lanhelin (Britanny). A tensile crack was produced by a compressive force applied on two opposite sharp edges carved in the middle of two facing sides (the initial block size is $25 \times 25 \times 40 \text{ cm}^3$). Then, a silicon rubber molding of one of the fracture surfaces is made, and after that used as a template to fabricate transparent

epoxy casts of the original surface. A second silicon rubber mold of the epoxy molding is then produced to obtain a perfectly matching surface (dimensional deformations during polymerization are much smaller for the silicon than for the epoxy). This method is widely used and reproduction problems are negligible for the present application [Auradou *et al.*, 2001; Yeo *et al.*, 1998; Isakov *et al.*, 2001; Kostakis *et al.*, 2003]. The complementary epoxy and rubber surfaces are the walls of the model fracture used in the present work.

Prior to the experiments, $2D$ maps of the epoxy surfaces are obtained by means of a mechanical profilometer (770×760) points with a $250\mu m$ grid spacing and a $10\mu m$ vertical resolution [Boffa, 1998]. The differences in height between the highest and the lowest points of the surface is $\simeq 17 mm$ and the root mean square deviations of the surface heights is $\simeq 3.5 mm$. As discussed in the introduction, *self-affine* surfaces have a roughness which does not contain any intrinsic wavelength, and it can be shown that the power spectral density $P(f)$ of the heights, for a linear profile drawn on the surface, should verify the following scaling law with the spatial frequency f :

$$P(f) \sim A \times f^{-1-2\zeta}. \quad (2)$$

Such spectral densities $P(f)$ obtained for the surface samples are plotted in Fig. 1, and follow indeed a power law as a function of f . The computed spectral densities showed no dependence, within experimental error, on the orientation of the profile used to compute them, which implies that the fractures are isotropic in their mean plane. By averaging spectra obtained for several orientations of the profiles, one obtains $\zeta = 0.75 \pm 0.05$, in agreement with previous studies of granite fractures [Boffa, 1998; Méheust and Schmittbuhl, 2000; Auradou *et al.*, 2001]. As indicated by the solid line with arrows at both ends in Figure 1, $P(f)$ follows this power law over approximately two decades :

the corresponding length scales range from 50 *mm* down to 0.75 *mm*. The lower limit f_m of this range is set by the resolution used in the present map; previous measurements have shown that the self-affine description remains valid at lower length scales, of the order of 0.1*mm* or less [Boffa, 1998]. The upper limit f_M arises from the reduced number of wavelengths which describe the surface topography at large scales: f_M is thus related to the finite size of the sample, which has a large-scale topography dominated by a few large undulations. This statistical effect usually becomes apparent at length scales greater than one fourth of the system size [Méheust and Schmittbuhl, 2000].

2.2. Experimental procedure and image analysis

The objective of the experiments is to analyse the flow inside an open fracture by monitoring the radial spreading of an injected dye. Using a radial injection geometry allows to estimate variations of the permeability of the fracture with the flow direction from asymmetries in the shape of the invaded zone. The two complementary surfaces are initially brought into full contact, with their mean plane (x, y) horizontal. The top (transparent) surface, see Fig. 2 for details, is kept fixed thereafter and the lower one can be translated while remaining precisely parallel to its initial orientation. Specifically, it is first displaced downwards ($-z$ direction) by a distance a_0 to open the fracture and then laterally in the (x, y) plane to the required location. This lateral displacement \vec{u} is small enough so that the two surfaces do not come in contact.

The fracture model is then placed inside a leak tight basin which is filled with transparent fluid in order to saturate the model prior to the experiments. Transparent fluid is then injected through a hole in the top surface and flows radially outwards. Once a steady flow is reached, a dyed fluid is injected and pictures of the invaded region are taken at

constant time intervals using a high resolution cooled 12 bits digital camera. Each pixel corresponds to a $250\mu m \times 250\mu m$ area. The fluids used are water-glycerol solutions with 10% glycerol. 0.2-0.3 g/l of nigrosine are added to the dyed solution and the density of the two fluids is matched by adding an equivalent amount of *NaCl* to the transparent solution. In order to avoid density differences due to temperature variations the solutions are stored at the same temperature. In all experiments density differences between the two fluids were always smaller than $25 \cdot 10^{-4} \text{ g/cm}^3$.

The dye concentration map is determined for each image obtained during the experiment by assuming the validity of Beer-Lambert's law. In this case, the light intensity $I(x, y)$ at a given point (x, y) of the image should vary exponentially both with the local aperture $a(x, y)$ and the local concentration $c(x, y)$ with:

$$I(x, y) = I_0(x, y) \exp(-2 \mu c(x, y) a(x, y)), \quad (3)$$

in which $I_0(x, y)$ is the light intensity for transparent fluid and μ is the extinction coefficient. The validity of this relation has been verified by opening the fracture without introducing a lateral shift so that the local aperture $a(x, y)$ is constant and equal to the vertical displacement Δz . The corresponding light intensity $I(x, y)$ was then determined for different dye concentrations c_0 and different mean apertures $a_0 = \Delta z$. All the corresponding results collapses into a single curve by plotting the ratio $I(x, y)/I_0(x, y)$ as a function of $\Delta z \times c_0$ and in a log-linear scale the variation is linear, as expected, for $a(x, y)c_0 < 0.15 \text{ g/m}^2$ ($\mu = 2.9 \pm 0.4 \text{ m}^2/\text{g}$). Using this result, and Eq. 3, the local, instantaneous concentration $c(x, y, t)$ during the displacement experiments can be determined

from the following relation:

$$\frac{c(x, y, t)}{c_f} = \ln \left[\frac{I(x, y, t)}{I_0(x, y)} \right] / \ln \left[\frac{I_0(x, y)}{I_f(x, y)} \right]. \quad (4)$$

Figure 3a displays a typical concentration map obtained in this way for an experiment in which the fracture walls are translated relative to each other parallel to the arrow. In addition to the irregularity of the front boundary, already discussed by *Auradou et al.* [2001] and by *Drazer et al.* [2004], its global shape is clearly anisotropic with a strong elongation in the direction perpendicular to the shear displacement \vec{u} . A similar anisotropy is observed on the aperture field displayed in Figure 3b, with the appearance of elongated channels, also perpendicular to \vec{u} .

2.3. Quantitative characterization of anisotropy and relation to permeability field

The anisotropy of the invaded zone can be characterized quantitatively from the inertia tensor $\mathbf{M}(t)$ of the concentration distributions. $\mathbf{M}(t)$ is computed using the definition :

$$\mathbf{M}(t) = \frac{1}{c_f} \sum c(x, y, t) \begin{pmatrix} y_*^2 & -x_* \times y_* \\ -x_* \times y_* & x_*^2 \end{pmatrix}, \quad (5)$$

The sum is taken over all pixels in the image and $x_* = x - x_c$ and $y_* = y - y_c$ where (x_c, y_c) is the center of mass of the invasion pattern. The eigenvalues λ_+^2 and λ_-^2 of the tensor $\mathbf{M}(t)$ and the corresponding principal axes are then determined: they characterize the magnitude of the anisotropy and the directions of fastest and slowest flow, respectively.

More quantitatively, the tensor $M(t)$ may be used to estimate the ratio between the permeabilities for flow along these two directions. If we ignore the surface roughness and consider a two dimensional Hele-Shaw flow with *weak* anisotropy in the permeability, $k_x \neq k_y$ but $|k_x - k_y| \ll (k_x + k_y)$, we can indeed compute the average elliptical shape

of a convected tracer front as follows. Assume liquid is injected through a small hole of radius r_0 at pressure p_0 , and allowed to escape at the circular outer boundary $r = r_1$ at atmospheric pressure $p_1 \equiv 0$. The velocities are

$$v_x = k_x \frac{\partial p}{\partial x} \quad \text{and} \quad v_y = k_y \frac{\partial p}{\partial y}, \quad (6)$$

which together with the incompressibility condition $\nabla \cdot \vec{v} = 0$ gives

$$k_x \frac{\partial^2 p}{\partial x^2} + k_y \frac{\partial^2 p}{\partial y^2} = 0. \quad (7)$$

To leading order in the permeability contrast, the pressure is readily found to be

$$p(r, \theta) = \frac{p_0}{\ln(r_0/r_1)} \left[\ln(r/r_1) + \frac{k_x - k_y}{2(k_x + k_y)} \times \left(\frac{r^2 - r_0^2 - r_1^2 + r_0^2 r_1^2 / r^2}{r_0^2 + r_1^2} \right) \cos 2\theta \right]. \quad (8)$$

Thus, to leading order in the permeability contrast, one has $v_x \sim k_x x/r^2$, and a similar relation for v_y . The location of the right-most end of the tracer ellipse, $(x_R, 0)$, has then a velocity $dx_R/dt \sim k_x/x_R$ so that $x_R^2(t) \sim k_x t$; similarly, the coordinate of the top end of the tracer ellipse verifies $y_T^2(t) \sim k_y t$. The ratio of the squares of the major and minor axes of the tracer ellipse, and therefore of the eigenvalues λ_+^2 and λ_-^2 , is equal to the ratio of the permeabilities for flow parallel to these axis:

$$\left(\frac{\lambda_+}{\lambda_-} \right)^2 = \frac{k_\perp}{k_\parallel} \quad (9)$$

3. Analysis of the experimental results

In this section we apply the procedures described above to determine the permeability anisotropy from the shape of the invasion pattern during the radial injection of a dyed fluid that displaces a transparent one. Several tracer injection experiments were performed for a fixed mean aperture $a_0 = 1 \text{ mm}$, and different shear-displacements in both x and y

directions. Reference test experiments with no shear displacement between the fracture walls were also performed to check that aperture variations are statistically isotropic (in this case, a roughly circular shape of the invaded zone is expected for a radial injection).

The direction of the maximum flow velocity is associated to the principal axis of the inertia tensor $\mathbf{M}(t)$ with the largest eigenvalue. Figure 4 displays the variation of the angle ϕ of this axis with x as a function of the radius of gyration R_g of the invasion pattern. R_g verifies $R_g^2 = \text{tr}(\mathbf{M})$ and increases approximately as the square root of time as required by mass conservation.

The data in Fig 4 correspond to different magnitudes and orientations of the shear displacement \vec{u} . In the case of non-zero shear displacements oriented parallel to the y axis (dark symbols), the angle ϕ remains close to zero, with an average over all data equal to 2.5° and variations of the order of $\pm 5^\circ$ around that value. In addition, the curves corresponding to larger amplitudes of the shear displacement ($|\vec{u}| = u_y$ varying from 0.5 to 1 mm) are all very similar. The elongation of the invaded zone is therefore, as expected, globally perpendicular to the lateral shift.

Analogous results are obtained for displacements parallel to the x axis (open symbols) and at an angle of -45° from it (* symbols). In these cases, ϕ is of the order of 90° and 45° , respectively, indicating again that the invaded zone is elongated perpendicularly to the displacement. This demonstrates that the flow anisotropy is directly connected to the lateral shift, with the preferential direction of flow oriented at an angle of 90° with respect to the direction of the shear displacement: this anisotropy does not arise therefore from any intrinsic feature in the fracture surface itself.

These results are in agreement with qualitative observations of the aperture fields, such as that presented in Fig. 3: the shear displacement creates ridges in the aperture field oriented in the perpendicular direction and partly inhibiting the flow. These conclusions are of course only valid if the shear displacement is different from zero. In the absence of such shear-displacement we observe, in some cases, a large dispersion in the measured values of ϕ , as expected for a nearly circular invaded zone for which ϕ is undetermined. In other experiments, ϕ is much less dispersed, possibly due to a residual lateral shift.

While ϕ indicates the orientation of the anisotropy, its magnitude is characterized by the ratio of the eigenvalues of the inertia tensor, λ_+/λ_- . The variation of λ_+/λ_- with the radius of gyration R_g of the invaded zone is displayed in Figure 5 : λ_+/λ_- reaches a roughly constant value for $R_g > 30 \text{ mm}$, suggesting that the growth of the invaded zone is self-similar. This asymptotic value of λ_+/λ_- represents then a robust parameter to characterize the anisotropy of the permeability for a given orientation and amplitude of the shear displacement.

Figure 5b also demonstrates that, for a fixed amplitude of the shear displacement, its orientation may influence λ_+/λ_- . When the displacement is applied along a given orientation either in the positive or negative direction, the effect on the ratio λ_+/λ_- is weak. On the other hand, its magnitude is somehow affected by changes in the orientation: $\lambda_+/\lambda_- \simeq 1.05$ for \vec{u} oriented along the x axis, but it reaches 1.15 when the shear displacement is applied in the y direction. These fluctuations come from the statistical character of the distribution of the ridges that alter the flow: they vary not only from sample to sample, but also with the orientation of \vec{u} . On the other hand, for a given orientation, the variation of λ_+/λ_- with the magnitude of the shear displacement $|\vec{u}| = u$ is smooth,

suggesting that the location of the main ridges remains the same as u increases. These results on λ_+/λ_- may be translated into permeability ratio by means of equation 9, which allows then for comparisons with the numerical simulations discussed below.

4. Theoretical discussion of the relation between permeability anisotropy and aperture field

The self-affine nature of the fracture walls affects the void distribution between them, and also plays an important role in fluid flow due to the hydrodynamic boundary conditions imposed there. Here we consider two complementary fracture surfaces with their mean planes parallel and horizontal, which can be separated vertically in order to open the fracture and shifted horizontally to introduce a shear displacement. For a vertical separation a_0 and shear displacements u_x and u_y along the x and y directions, respectively, the local aperture is defined as the vertical distance separating the two walls and is given by :

$$a(x, y) = h(x, y) - h(x - u_x, y - u_y) + a_0. \tag{10}$$

The covariance of the aperture was obtained previously (using Eq. 1), and two distinct scaling regimes were found [Plouraboué *et al.*, 2000]. For distances smaller than the shear displacement, the aperture field was shown to have self-affine correlations with exponent ζ , while for larger distances, the covariance decreases with the distance. The magnitude of the shear displacement thus represents a crossover length scale, and can be regarded as the typical size of features in the aperture distribution. Considering the self-affine scale invariance, the aperture variance, $\sigma_a^2 = \langle (a(x, y) - a_0)^2 \rangle$, for a shear displacement of size u is simply given by $\sigma_a(u) = Cu^\zeta$, where C is related to the amplitude of the roughness of the fracture wall. Figure 6 demonstrates this power law behavior for different orientations

of the shear displacement directions. For all the chosen orientations σ_a varies with u with an exponent $\zeta = 0.75$, in agreement with the Hurst exponent measured in Sec. 2.1 ($\zeta = 0.75 \pm 0.05$).

In the following, we use the ratio $S \equiv \sigma_a(u)/a$ as a parameter to quantify the normalized fluctuations in the local aperture introduced by the shear displacement: when $S \ll 1$, the aperture irregularities are a small perturbation on a nearly-constant aperture field (note that in the absence of shear displacement between the surfaces the aperture is constant and equal to a_0 throughout the fracture) and their effect on the flow is negligible, but as S approaches 1 the channel becomes quite convoluted and local aperture variations must be considered to correctly describe the flow properties.

A second important earlier result is that the aperture correlation length is anisotropic, being smaller in the shift direction than in the orthogonal direction by a numerical factor of $2\zeta - 1 < 1$ [Roux *et al.*, 1998]. The effect of such an anisotropy on the flow in rough fractures was studied numerically by *Thompson and Brown* [1991], who demonstrated that the permeability along the direction of the largest correlation length is enhanced while flow parallel to the direction of the smallest correlation length is inhibited. The effect was related to the occurrence of large ridges oriented along the largest correlation length direction, i.e. in the direction perpendicular to the shear displacement, and in fact such large structures are observed in our system, as can be seen in Figure 3.

This description can be used to motivate a model for the permeability anisotropy which considers the parallel ridges to provide parallel flow channels, which are in series with respect to the direction of the shift [Zimmerman and Bodvarsson, 1996]. Flow parallel to the shift is then analogous to electrical current flow through resistors in series and the

equivalent hydraulic aperture is $\langle a^{-3} \rangle^{-1}$, whereas flow perpendicular to the shift is analogous to resistors in parallel where the equivalent aperture is $\langle a^3 \rangle$. Specifically, assuming that the distribution of apertures is Gaussian, one can evaluate the two averages involved, yielding the upper and lower bounds

$$\frac{\langle a^3 \rangle}{a_0^3} = 1 + 3S^2, \tag{11}$$

and

$$\frac{\langle a^{-3} \rangle^{-1}}{a_0^3} = 1 - 6S^2 - 9S^4 + O[S^6], \tag{12}$$

respectively, in the limit $S \ll 1$.

Before applying this prediction to the experimental data, we shall first evaluate them on the results of simulations performed on numerical models of self-affine fractures. These models allow for an easier testing of the variability of the results from a fracture sample to another. They also allow to determine separately the permeabilities for flow parallel and perpendicular to the displacement vector \vec{u} , while the experiments only allow to determine the ratio of these two permeabilities.

5. Numerical procedure

A first issue is the choice of the flow computation technique. When the local aperture of the fracture varies slowly along the fracture plane, the lubrication, or Reynolds, approximation can be used to describe the flow in the fracture [*Méheust and Schmittbuhl, 2000*]. On the other hand, many studies have pointed out that, for natural fractures, this approximation fails to give an accurate description of the hydraulic properties [*Yeo et al., 1998; Nicholl et al., 1999; Dijk and Berkowitz, 1999; Konzuk and Kueper, 2004*]. In fact, when the roughness of the walls becomes non-negligible compared to the mean aperture

of the fracture, e.g. when the surfaces are close to contact, the lubrication approximation fails, and a complete description of the flow field, which accounts for the flow velocity normal to the surface, is needed [Mourzenko *et al.*, 1995; Drazer and Koplik, 2000]. The lattice Boltzmann technique has therefore been selected to compute the flow because of its good adaptation to 3D complex geometries.

First, a self-affine surface is generated numerically, using a Fourier synthesis method [Drazer and Koplik, 2002], and the fracture pore space is modeled as the region between one such surface and a suitably translated replica. In order to mimic the experimental procedure, the two complementary surfaces are first assumed to be separated by a fixed distance a_0 in the direction z normal to the mean plane of the fracture. Then, a shear displacement of the upper surface is introduced in the (x, y) plane. The maximum shear displacement investigated in each direction corresponds to the occurrence of the first contact point between the two surfaces and, therefore, the fracture remains open over its full area. In order to compare the numerical results to the experiments, both the Hurst exponent and the average magnitude of the surface roughness need to be matched to their experimental values: the average fluctuations in surface height over a distance of 1 mm was thus been set to 0.25 mm, and the Hurst exponent ζ was set to 0.8. Finally, the mean aperture was set to $a \simeq 1\text{mm}$, which is comparable to that used in the experiments. Using these values, the local height varies considerably over distances of the order of the aperture size so that computing the complete flow field inside the fractures is required.

In order to capture the three-dimensional character of the flow field inside the fractures large cubic lattices, with as many as $1024 \times 1024 \times 20$ sites, are used in the simulations. Hence, the lattice spacing δ corresponds to 0.05 mm (the mean aperture $a_0 = 1\text{mm}$

corresponds to 20 lattice sites). The Lattice Boltzmann method is then used to compute the flow field in the presence of a pressure gradient and using periodic boundary conditions in the plane of the surface (see *Drazer and Koplík* [2000] for details of the simulation method). The pressure gradient is applied both along and perpendicular to the shear displacement between surfaces. In addition, and to avoid the possible effects of any intrinsic anisotropy in the generation of the self-affine surfaces, the shear displacements are introduced in both the x and y directions within the mean plane. The Reynolds number in the simulations is $\text{Re} = Ua/\nu \sim a^3\rho\nabla P/12\nu^2 < 1$ for $a = 1\text{mm}$, where we used the parallel plane approximation to estimate U . Inertia effects are therefore negligible [*Skjetne et al.*, 1999], and the flow is governed by the linear Stokes equations, which are invariant under velocity rescaling. Then, by computing the flow rate, we can obtain the permeability of the fracture and its dependence on the magnitude and orientation of the shear displacement.

6. Analysis of the numerical simulations

Numerical simulations are performed in configurations reproducing as far as possible those encountered in the experiments. Several series of computations were performed on self-affine fracture models for different mean apertures ($0.5 < a_0 < 2.0\text{mm}$) and shear-displacements \vec{u} ($0 < u < 1.6\text{mm}$). The displacement \vec{u} is oriented along directions x or y in the mean plane of the surfaces and the size of the simulated fractures is typically $25.6 \times 25.6\text{mm}$. For given values of a_0 and \vec{u} , computations are performed on 10 independent realizations in order to estimate the dispersion of the results (only a part of the corresponding data will be displayed for clarity but all the data is consistent with the trends visible on the figures).

Figure 7 displays the variation of the normalized permeabilities k_{\parallel}/k_0 (resp. k_{\perp}/k_0) as a function of the normalized aperture variance S^2 for a constant mean aperture $a_0 = 1.0 \text{ mm}$ and for displacements either along x or along y . k_0 is the isotropic permeability for $u = 0$ and k_{\parallel} and k_{\perp} are the respective permeabilities for flow parallel and normal to the shear displacement. The normalized variance S^2 is used as the horizontal scale since, as already discussed in Sec. 4, it is the relevant parameter to characterize the dependence of the permeability on the shear-displacement (the magnitude u of the shear displacement ranges between 0 and 1.6 mm).

The key feature is the fact that k_{\perp}/k_0 and k_{\parallel}/k_0 both vary linearly with S^2 but in opposite directions (k_{\perp}/k_0 increases with S^2 while k_{\parallel}/k_0 decreases). Figure 7 also shows that this linear variation is observed for shear displacements \vec{u} oriented both parallel to x and y axes, which demonstrates that the permeability anisotropy is induced by the shear displacement and it is not associated to geometrical anisotropies present before the relative displacement of the walls.

These linear variations of the permeability qualitatively agree with the simple model presented in Sec. 4. In fact, in Sec. 4 we estimated the upper bounds for the variations of k_{\perp}/k_0 and k_{\parallel}/k_0 with S^2 (see Eqs. 11 and 12), which are represented by solid lines in Fig. 7. As can be seen, the sign and order of magnitude of these variations are the same as those of the numerical simulations.

Another interesting result is the strong correlation between the variations of k_{\parallel}/k_0 and those of k_{\perp}/k_0 : fractures displaying a large reduction of the permeability k_{\parallel} are generally the same that display a significant increase of k_{\perp} .

Finally, other simulations were performed in which S^2 is modified by varying the mean aperture from $a_0 = 2.0$ mm to $a_0 = 0.75$ mm, while keeping the shear displacement constant, $u = 1.5$ mm. In this case, the variance S^2 increases when the aperture a_0 decreases. The variations of k_{\parallel}/k_0 and k_{\perp}/k_0 as a function of S^2 for sets of data obtained in this way for three different realizations of the fracture surface are plotted in Fig. 8. One observes the same general trend as when a_0 is kept constant and u varies like in Fig. 7 : k_{\parallel}/k_0 decreases and k_{\perp}/k_0 increases or remains constant as a_0 is reduced and S^2 increases. For a given realization of the surface, the variations of k_{\parallel}/k_0 and k_{\perp}/k_0 with S^2 are linear and both remain within the bounds set by Eqs. 11 and 12. This confirms that the normalized aperture variance, S^2 , is indeed the adequate parameter to characterize the disorder in the aperture field introduced by the shear displacement between the two surfaces.

Numerically, 10 self-affine surfaces were generated and were used to create aperture fields for different mean apertures and shear displacements. In average, fitting the permeability values to a quadratic dependence on S over all the realizations we obtain:

$$\left\langle \frac{k_{\perp}}{k_0} \right\rangle = 0.995 + 1.09S^2, \quad (13)$$

and

$$\left\langle \frac{k_{\parallel}}{k_0} \right\rangle = 0.955 - 3.05S^2. \quad (14)$$

Nevertheless, large fluctuations are observed from one realization to another: for some the wall roughness only weakly perturbs the flow while for some others the roughness strongly distorts the flow and the permeability behaves as predicted by Eqs. 11 and 12.

7. Comparison between experiments and simulations

As discussed in Sec. 2.3, the analysis of the geometry of the invasion pattern in the injection experiments allows one to estimate the ratio k_{\perp}/k_{\parallel} of the permeabilities for flow perpendicular and parallel to the shear displacement \vec{u} . The variance S^2 of the aperture can be computed for each set of values of a_0 and \vec{u} from the profilometer maps of the fracture surfaces (see Sec. 2.1). It is therefore possible to determine experimentally both k_{\perp}/k_{\parallel} and S^2 for each experiment. Figure 9 displays the variations of the permeability ratio as a function of S^2 , as determined from the shape of the invasion front in a series of injection experiments (see Sec. 2.3). Three sets of experiments are presented, two of them correspond to shear displacements oriented along the x-direction or y-direction. No distinction between the positive or negative direction is made since, as point out in Sec. 3, the permeability ratio is roughly independent of the shear displacement sign, but only on its magnitude and orientation. The third set represent experiments performed with a fixed shear displacement, $u_x = 2.0$ mm, and a variable aperture a_0 ranging from 1.25 mm to 2.0 mm. As it can be seen in Fig. 9, the permeability ratios measured with a variable aperture and a shear displacement oriented along the x -direction are aligned with those obtained with a fixed aperture and a variable shear displacement applied along the x -direction.

Independently of the shear-displacement direction the permeability ratio increases roughly linearly with S^2 and its values remain bellow the upper bond provided by combining Eqs. 11 and 12. We also show that the permeability ratios obtained from the experiments always lie between the strongest and weakest anisotropies observed in the very extensive numerical computations. When $S \sim 0.1$, a departure of k_{\perp}/k_{\parallel} from a linear behavior is observed in the numerical simulations. This result is consistent with

the model discussed in Sec. 4, which is clearly no longer valid for $S \gtrsim 0.13$, for which it predicts a closed fracture (zero permeability). A sharp decreases of the permeability along the shear displacement is thus expected and corresponds to a strong increases of k_{\perp}/k_{\parallel} when S can no longer be considered to be small compared to 1. This divergence is not observed experimentally since the method used for the anisotropy characterization is strictly valid for weak anisotropic permeabilities as discussed in Sec. 2.3.

Finally, we also present in Fig.9 a linear fit to the experimental data. Circumstantially, the strongest effect is observed when the walls are shift in the y-direction and a linear regression indicates an increased of k_{\perp}/k_{\parallel} with S^2 with a slope of 5.4 ± 0.3 . In the x-direction the permeability ratio also increased with S^2 but with a slope of 2.3 ± 0.15 .

8. Conclusions

The present study has confirmed both experimentally and numerically that the permeability of a fracture made of two complementary surfaces with a shear displacement \vec{u} is lower for flow parallel to \vec{u} than perpendicular to it. More precisely, the parallel permeability (k_{\parallel}) decreases significantly while the perpendicular one (k_{\perp}) increases or remains constant.

Qualitatively, this result appears to be related to the appearance of preferential channels of larger local aperture oriented perpendicular to \vec{u} : these channels are indeed visible on aperture images reconstructed from experimental (or numerical) profilometry maps. Assuming such a geometrical structure allows to develop simple theoretical predictions for the relation between the permeability variations and the normalized variance S^2 of the aperture field. The permeability for flow parallel (perpendicular) to \vec{u} was then shown to decrease (increase) approximately linearly with S^2 . The absolute magnitude of the

variation is also predicted to be two times larger for the parallel flow. These predictions are qualitatively correct and provide an estimation of the order of magnitude for the permeability variations and for the ratio of the permeabilities perpendicular and parallel to the shear displacement. In particular, both for the experiments and the numerical simulations, a linear variation for the permeability ratio with S^2 is actually observed - showing that the variance S^2 is a key parameter of the process. However there is a significant dispersion in the absolute value of the prefactors in these linear relations from one sample to another.

Further studies will be needed to understand the origin of the dispersion of the numerical values of the permeability variations and uncover the other characteristic geometrical parameters which may be involved in the process (finite size effects may be a limitation, particularly for the present simulations). Another important issue for practical applications is whether an estimation of the aperture variance can be obtained, for a given shift \vec{u} and mean aperture a_0 of the fracture without requiring to map the full surface of the sample.

Acknowledgments. We are indebted to S. Bourles for providing us with the fracture moldings and to G. Chauvin, R. Pidoux and C. Saurine for their assistance in the realization of the experimental set-up. Computer resources were provided by the National Energy Research Scientific Computing Center. HA and JPH are supported by the CNRS and ANDRA through the GdR FORPRO (contribution No. 2004/20) and the EHDRA (European Hot Dry Rock Association) and PNRH programs. GD and Jk are supported by the Geosciences Program of the Office of Basic Energy Sciences (US Department of

Energy), and by a PSC-CUNY grant. This work was facilitated by a CNRS-NSF Collaborative Research Grant.

Notes

1. There is a direct analogy between the variance in the surface heights and the random walk problem. A standard random walk corresponds to a Hurst exponent $\zeta = 0.5$ and a linear growth of the variance, whereas a Hurst exponent $\zeta = 0.8$ corresponds to an anomalous hipper-diffusive behavior [Feder, 1988].

References

- Adler, P. M., and J.-F. Thovert (1999), *Fractures and Fracture Networks*, kluwer Academic Publishers, Dordrecht, The Netherlands.
- Auradou, H., J. P. Hulin, and S. Roux (2001), Experimental study of miscible displacement fronts in rough self-affine fractures, *Phys. Rev. E*, *63*, 066306.
- Boffa, J.M., C. Allain and J.P.Hulin (1998), Experimental analysis of fracture rugosity in granular and compact rocks, *Eur. Phys. J. Appl. Phys.*, *2*, 281–289.
- Bouchaud, E. (2003), The morphology of fracture surfaces: A tool for understanding crack propagation in complex materials, *Surface Review And Letters*, *10*, 797–814.
- Dijk, P. E., and B. Berkowitz (1999), Three-dimensional flow measurements in rock fractures, *Water Resour. Res.*, *35*, 3955–3959.
- Drazer, G., and J. Koplik (2000), Permeability of self-affine rough fractures, *Phys. Rev. E*, *62*, 8076–8085.
- Drazer, G., and J. Koplik (2002), Transport in rough self-affine fractures, *Phys. Rev. E*, *66*, 026303.
- Drazer, G., H. Auradou, J. Koplik, and J. P. Hulin (2004), Self-affine fronts in self-affine fractures: Large and small-scale structure, *Phys. Rev. Lett.*, *92*, 014501.

- Feder, J. (1988), *Fractals*, Physics of Solids and Liquids, Plenum Press, New York.
- Gentier, S., E. Lamontagne, G. Archambault, and J. Riss (1997), Anisotropy of flow in a fracture undergoing shear and its relationship to the direction of shearing and injection pressure, *Int. J. Rock Mech. & Min. Sci.*, *34*(3-4), 412.
- Isakov, E., S. R. Ogilvie, C. W. Taylor, and P. W. J. Glover (2001), Fluid flow through rough fractures in rocks i: high resolution aperture determinations, *Earth Planet. Sci. Lett.*, *191*, 267–282.
- Kim, I., W. B. Lindquist, and W. B. Durham (2003), Fracture flow simulation using a finite-difference lattice boltzmann method, *Phys. Rev. E*, *67*, 046708.
- Konzuk, J. S., and B. H. Kueper (2004), Evaluation of cubic law based models describing single-phase flow through a rough-walled fracture, *Water Resour. Res.*, *40*, w02402.
- Kostakis, k., J. P. Harrison, and S. M. Heath (2003), Silicone rubber castings for aperture measurement of rock fractures, *Int. J. Rock Mech. Min. Sci.*, *40*, 939–945.
- Mandelbrot, B. B. (1983), *The Fractal Geometry of Nature*, W. H. Freeman, New York.
- Méheust, Y., and J. Schmittbuhl (2000), Flow enhancement of a rough fracture, *Geophys. Res. Lett.*, *27*(18), 2989–2992.
- Mourzenko, V., J. F. Thovert, and P. Adler (1995), Permeability of a single fracture; validity of the reynolds equation, *J. Phys. II*, *5*(3-4), 465–482.
- NAS Committee on Fracture Characterization and Fluid Flow (1996), *Rock Fractures and Fluid Flow: Contemporary Understanding and Applications*, National Academy Press, Washington, D.C.
- Nicholl, M. J., H. Rajaram, R. J. Glass, and R. Detwiler (1999), Saturated flow in a single fracture: Evaluation of the reynolds equation in measured aperture fields, *Water*

Resour. Res., *35*, 3361–3373.

Olsson, W. A., and S. R. Brown (1993), Hydromechanical response of a fracture undergoing compression and shear, *Int. J. Rock Mech. Min. Sci. & Geomech. Abs.*, *30*(7), 845–851.

Plouraboué, F., P. kurowski, J. P. Hulin, S. Roux, and J. Schmittbuhl (1995), Aperture of rough cracks, *Phys. Rev. E*, *51*(3), 1675–1685.

Plouraboué, F., J.M. Boffa, P. kurowski, J. P. Hulin and S. Roux (2000), Experimental study of the transport properties of rough self-affine fractures, *J. Cont. Hydro.*, *46*, 295–318.

Roux, S., F. Plouraboué, and J. P. Hulin (1998), Tracer dispersion in rough open cracks, *Transport In Porous Media*, *32*, 97–116.

Sahimi, M. (1995), *Flow and Transport in Porous Media and Fractured Rock: from classical methods to modern approaches*, Wiley-VCH, New York.

Skjetne, E., A. Hansen, and J. S. Gudmundsson (1999), High-velocity flow in a rough fracture, *Journal Of Fluid Mechanics*, *383*, 1–28.

Thompson, M. E., and S. R. Brown (1991), The effect of anisotropic surface roughness on flow and transport in fractures, *J. Geophys. Res.*, *vol.96, no.B13*(13), 21,923–21,932.

Yeo, I. W., M. H. De Freitas, and R. W. Zimmerman (1998), Effect of shear displacement on the aperture and permeability of a rock fracture, *Int. J. Rock Mech. & Min. Sci.*, *35*(8), 1051–1070.

Zimmerman, R. W., and G. S. Bodvarsson (1996), Hydraulic conductivity of rock fractures, *Transp. Porous Media*, *23*, 1–30.

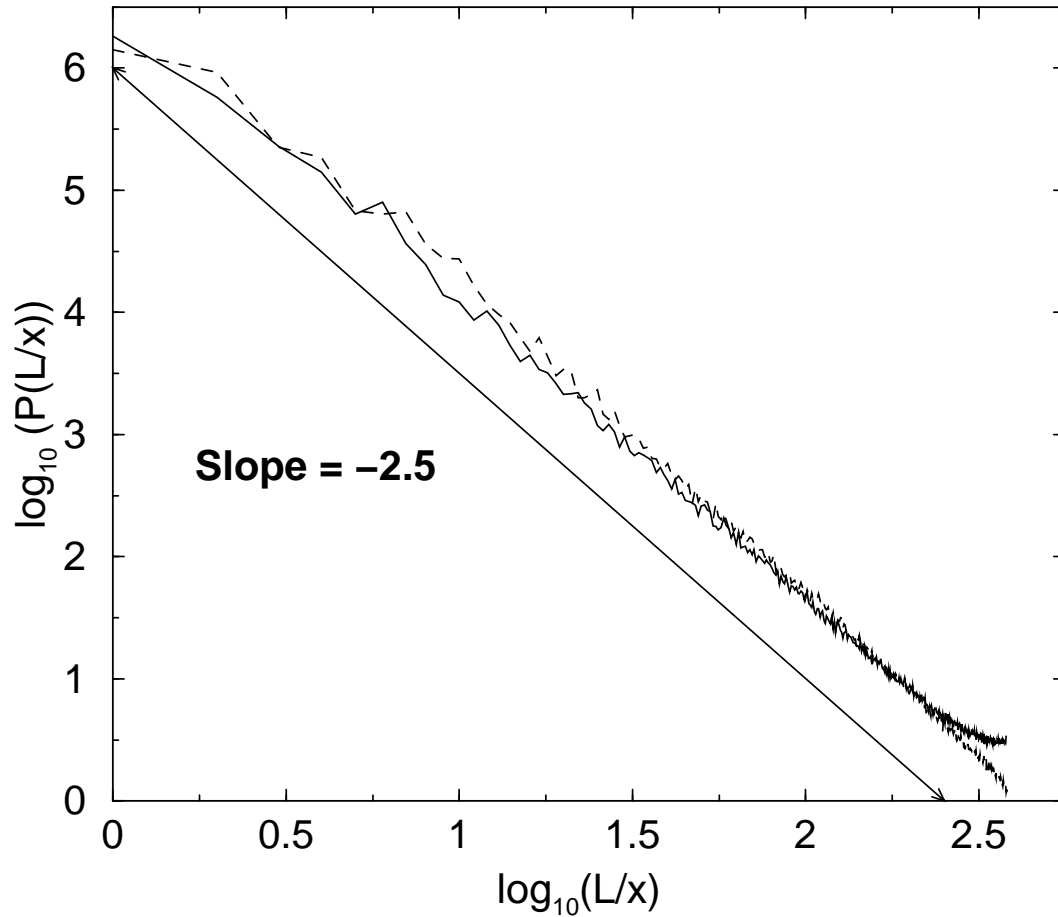


Figure 1. Power spectral density of the experimental fracture surfaces. The spatial frequencies are $f = L/(n\Delta x)$, for $n = 1, 2, \dots, L/\Delta x$, where $L = 20\text{cm}$ is the fracture length and $\Delta x = 250\mu\text{m}$ is the resolution length along the profile. The solid and dashed lines correspond to profiles obtained normal and parallel to the direction of crack propagation. The latter two curves are shifted vertically by 0.75 for visual clarity.

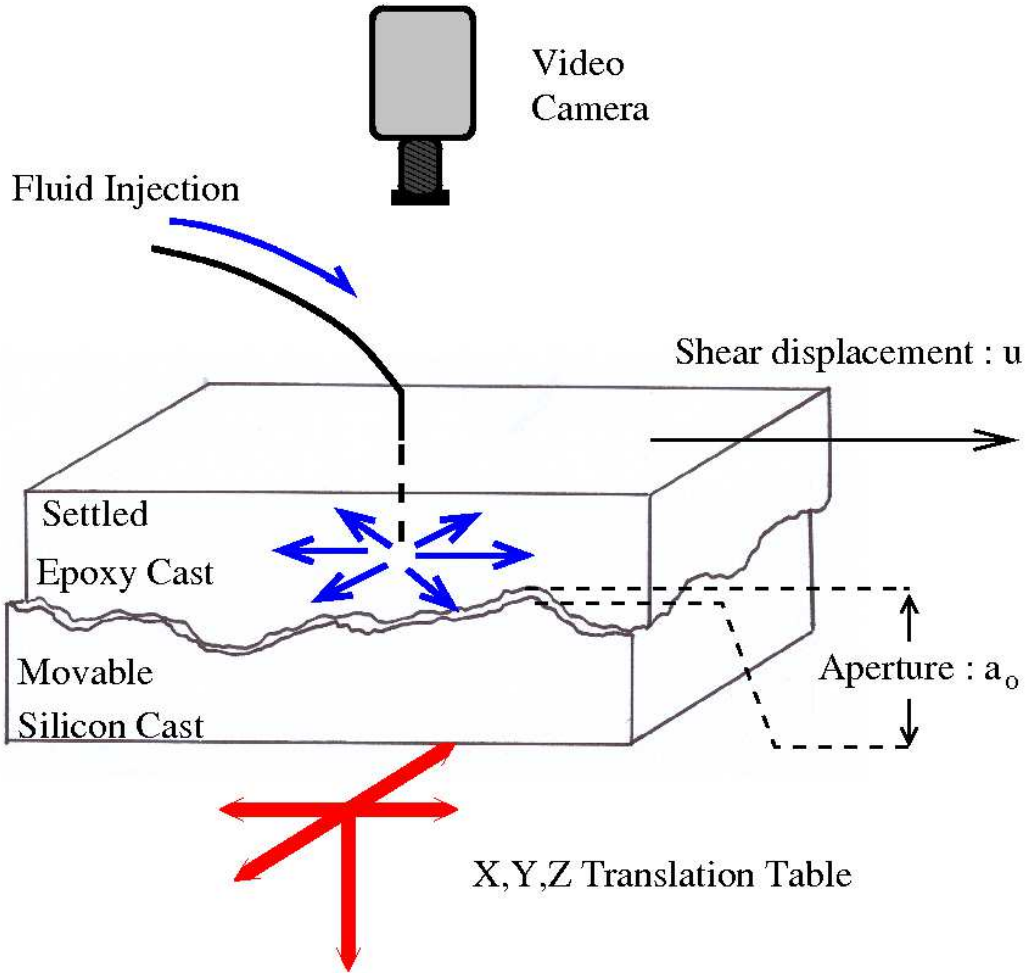


Figure 2. Schematic view of the experimental set-up. The top wall is a transparent epoxy cast and has a fixed position. The bottom wall is a silicone replica of the top wall and can be moved down and laterally. The dyed fluid is injected in a radial, divergent configuration and it displaces a non-dyed fluid which initially saturates the fracture gap. The flow process is visualized with a camera set above the fracture. The two controlled lengths are indicated: a_0 , the mean vertical separation between walls, and \vec{u} , the shear-displacement vector.

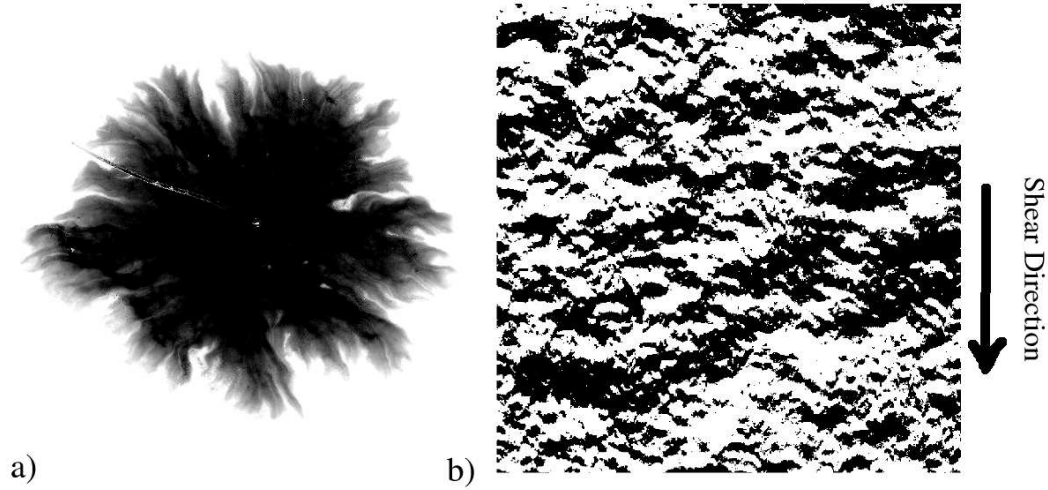


Figure 3. Example of the relation between flow anisotropy and aperture field in a sheared fracture, with $a_0 = 1.25 \text{ mm}$ and $u_y = 2.0 \text{ mm}$ (the direction of the shear displacement is indicated by the arrow). The normalized aperture variance is $S^2 = 0.133$. (a) Concentration map. (b) Aperture field computed using Eq. 4, where white corresponds to a local aperture $a(x, y) < a_0$ and black to $a(x, y) > a_0$.

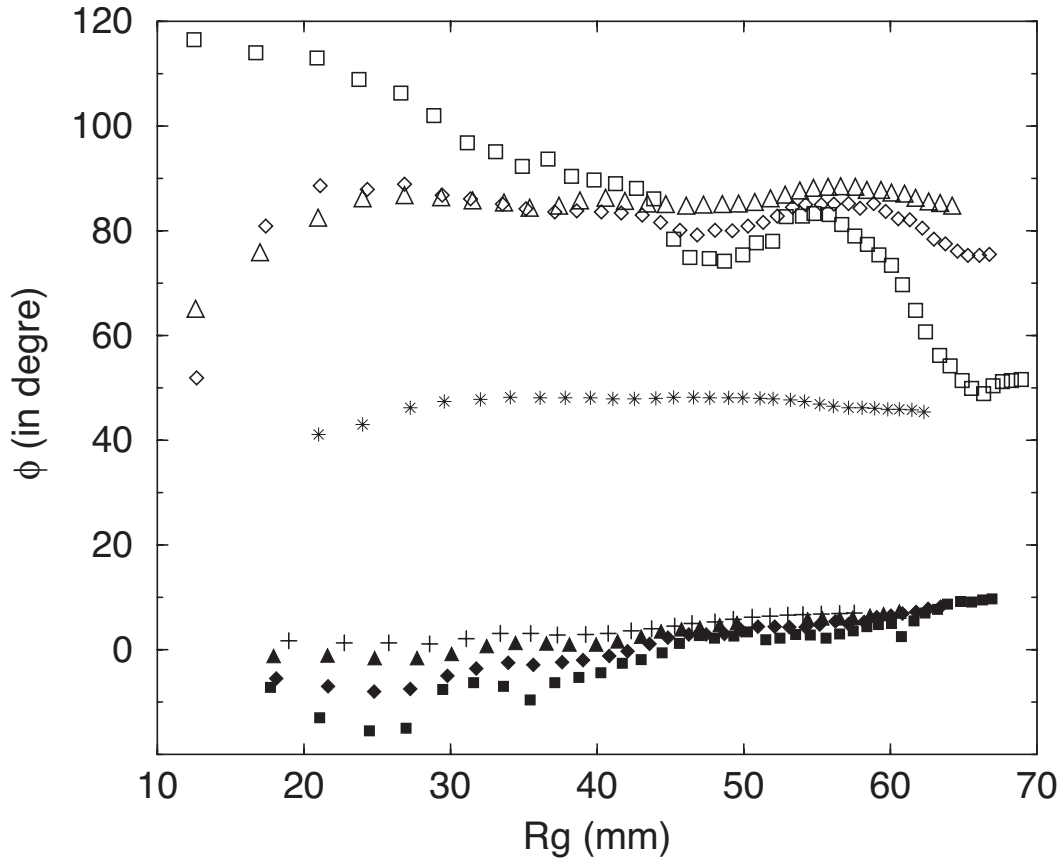


Figure 4. Angle ϕ between the x axis and the direction of maximum flow velocity for different shear displacements. \vec{u} parallel to x : $u = 0.25$ mm (\square), 0.5 mm (\diamond), 0.75 mm (\triangle); \vec{u} parallel to y : $u = 0.25$ mm (\blacksquare), 0.5 mm (\blacklozenge), 0.75 mm (\blacktriangle), 1 mm ($+$); \vec{u} at -45° from x , $u = 1$ mm ($*$).

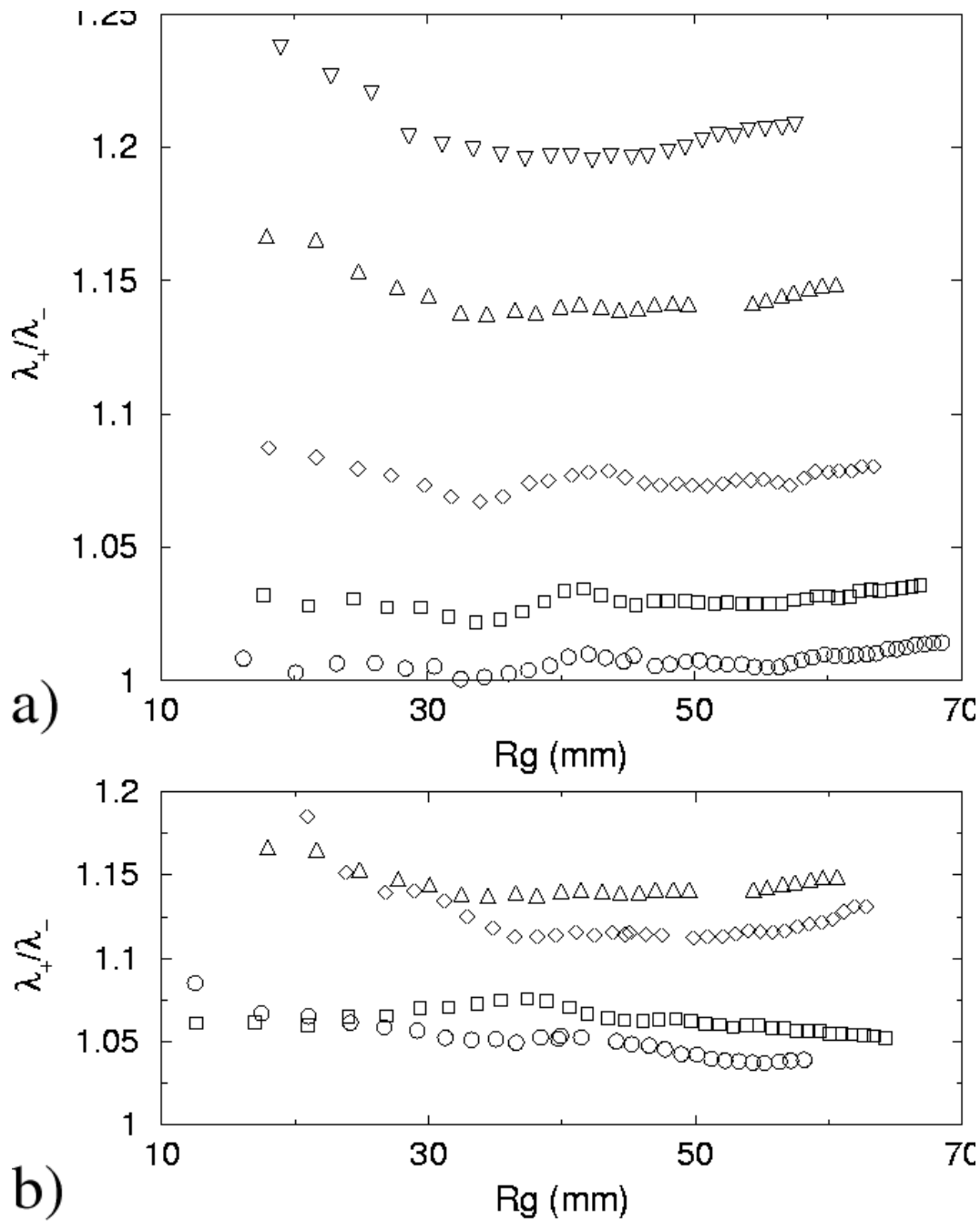


Figure 5. Experimental variation of the ratio λ_+/λ_- as function of the radius of gyration R_g of the invaded zone for a shear displacement \vec{u} oriented along $+y$ and with the following amplitudes : $u = 0$ (\circ), 0.25 mm (\square), 0.5 mm (\diamond), 0.75 mm (\triangle), 1 mm (∇). (b) Variation of λ_+/λ_- with R_g for a constant magnitude of the shear displacement \vec{u} ($u = 0.75$ mm) and oriented in the following directions: $+x$ (\circ), $-x$ (\square), $+y$ (\triangle), $-y$ (\diamond).

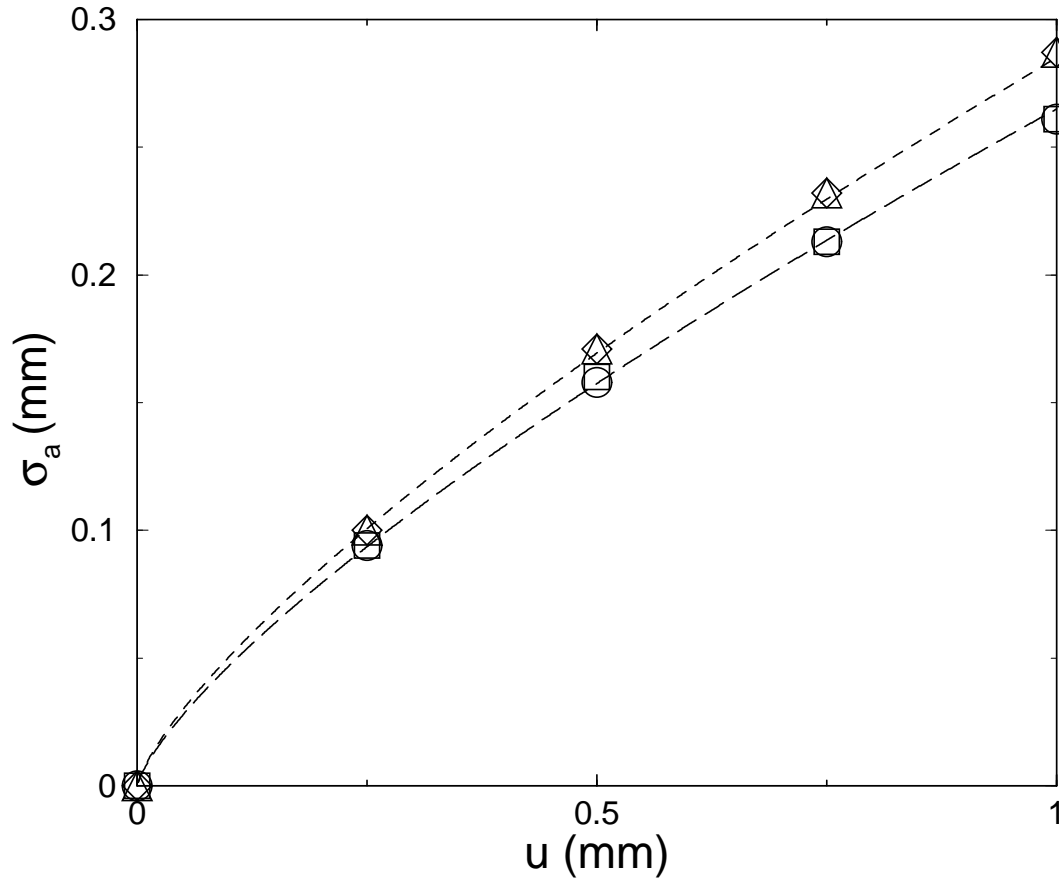


Figure 6. Variance of the aperture field, σ_a , as a function of the magnitude of the shear displacement, u , in directions : $+x(\square)$, $-x(\circ)$, $+y(\triangle)$, $-y(\diamond)$. Dashed line $\sigma_a = 0.285 u^{0.75}$ and Long dashed line : $\sigma_a = 0.265 u^{0.75}$.

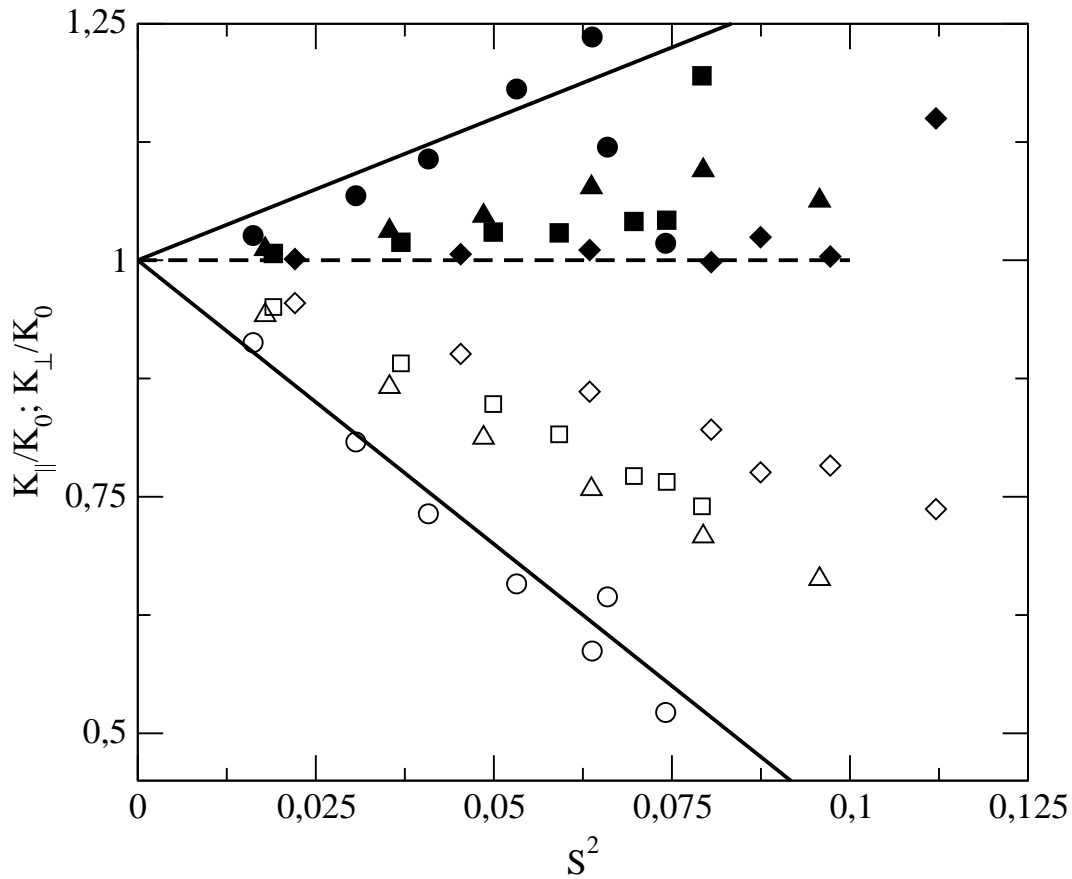


Figure 7. Permeability as a function of the shear displacement in self-affine fractures. Open (closed) symbols correspond to the permeability parallel (perpendicular) to the shear displacement $k_{||}/k_0$ (k_{\perp}/k_0) as a function of the normalized aperture variance S^2 . The symbols [(■, □) and (●, ○)] correspond to simulations performed in a single fracture but for two orthogonal directions for the shear displacement, that is $u_x \neq 0, u_y = 0$ and $u_x = 0, u_y \neq 0$, respectively. Analogously, the other four sets, [(◆, ◇) and (▲, △)] correspond to simulations performed in a single fracture and for two orthogonal orientations of the shear displacement. The upper (lower) solid line corresponds to the upper (lower) bound of the permeability given in Eq. 11 (Eq. 12).

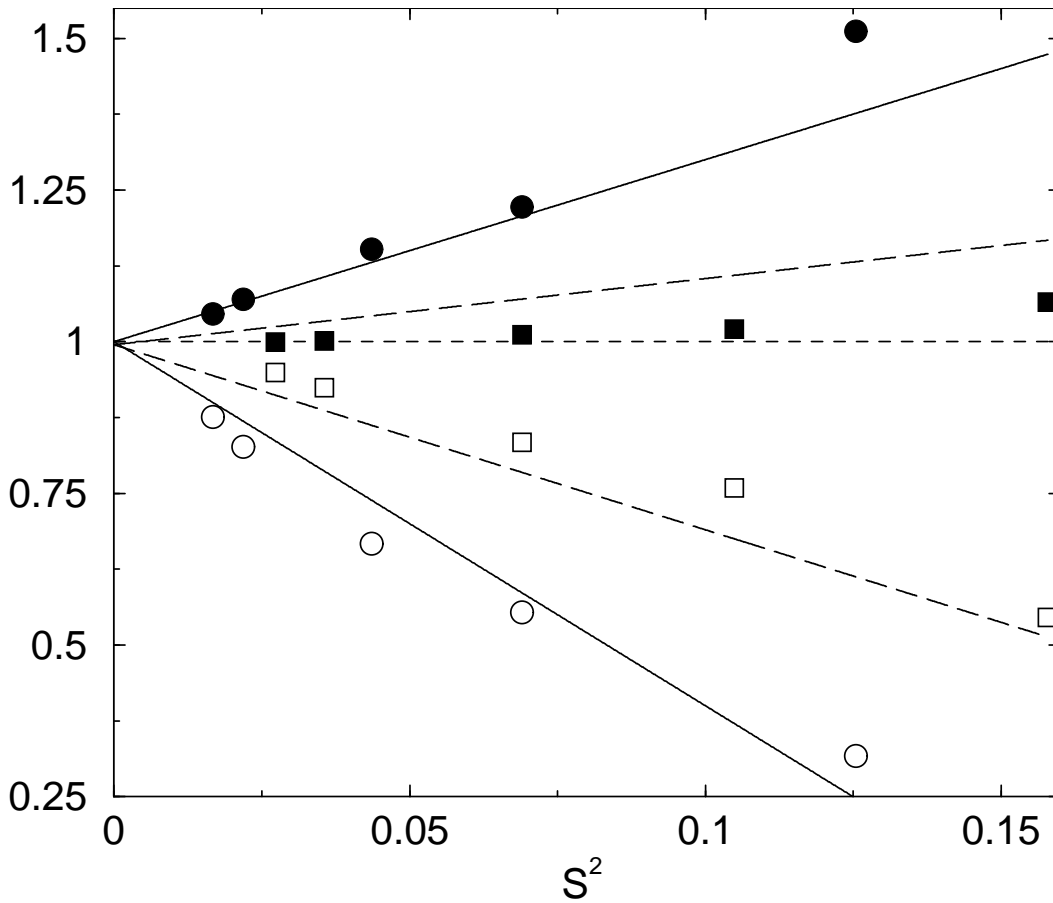


Figure 8. Normalized permeabilities k_{\parallel}/k_0 (open symbols) and k_{\perp}/k_0 (closed symbols) from two numerical simulations as a function of the normalized aperture variance S^2 . Simulations correspond to a fixed shear displacement $u_x = 1mm$ and variable aperture $0.75 < a_0 < 2.0$ mm. The upper (lower) solid line correspond to the upper (lower) bound for the permeability given in Eq. 11 (Eq. 12). The long dashed lines correspond to a linear fit of k_{\perp}/k_0 and k_{\parallel}/k_0 over all the numerical realizations.

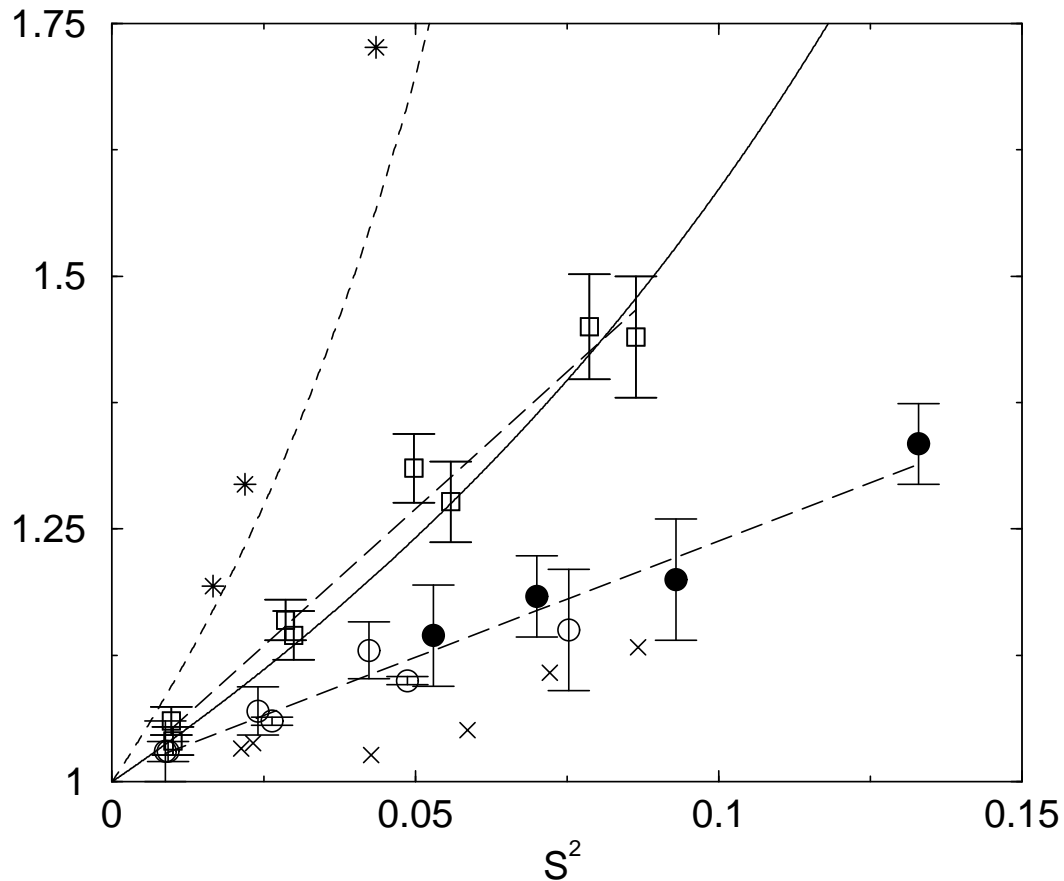


Figure 9. Permeability ratio k_{\perp}/k_{\parallel} as a function of the normalized aperture variance S^2 . (\square, \circ, \bullet) experimental data; (\star, \times) numerical data. \square symbols correspond to a shear displacement along the y axis (either in the positive or negative direction). \circ symbols correspond to a shear displacement along the x -direction with $a_0 = 1.0 \text{ mm}$, while \bullet symbols correspond to $u_x = 2.0 \text{ mm}$ and mean apertures ranging from 1.25 mm to 2 mm . \star and \times symbols correspond to numerical realizations showing the strongest and the weakest anisotropy, respectively. The dotted line corresponds to the upper bound for the permeability ratio estimated from Eqs. 11 and 12. The solid line corresponds to the permeability ratio $\langle k_{\perp}/k_{\parallel} \rangle$ averaged over all the numerical realizations. The long dotted lines corresponds to linear fits of the experimental data.

